A methodical calibration procedure for discrete element models

A Methodical Calibration Procedure for Discrete Element Models

Michael Rackl[a,*], Kevin J. Hanley[b]

[a] *Institute for Materials Handling, Material Flow and Logistics, Technical University of Munich, Boltzmannstraße 15, 85748 Garching, Germany*

[b] *Institute for Infrastructure and Environment, School of Engineering, The University of Edinburgh, Edinburgh EH9 3JL, UK*

Abstract

Researchers and engineers have widely adopted the discrete element method (DEM) for simulation of bulk materials. One important aspect in such simulations is the determination of suitable material and contact law parameters. Very often, these parameters have to be calibrated because they are difficult to measure or, like rolling friction, do not have a physical analogue. Moreover, coarse-grained particle models are commonly used to reduce computational cost and these always require calibration. Despite its disadvantages, trial and error remains the usual way to calibrate such parameters. The main aim of this work is to describe and demonstrate a methodical calibration approach which is based on Latin hypercube sampling and Kriging. The angle of repose and bulk density are calibrated for spherical glass beads. One unique feature of this method is the inclusion of the simulation time-step in the calibration procedure to obtain computationally efficient parameter sets. The results show precise calibration outcomes and demonstrate the existence of a solution space within which different parameter combinations lead to similar results. Kriging meta-models showed excellent correlation with the underlying DEM model responses. No correlation was found between static and rolling friction coefficients, although this has sometimes been assumed in published research. Incorporating the Rayleigh time-step in the calibration method yielded significantly increased time-step sizes while retaining the quality of the calibration outcome. The results indicate that at least particle density, Young's modulus and both rolling and static friction coefficients should be used for calibration; trial-and-error would be highly inefficient for this number of parameters which highlights the need for systematic and automatized calibration methods.

Keywords: discrete element method, calibration, optimization, Kriging, Latin hypercube sampling, material test

1. Introduction

Although the discrete element method (DEM) was developed in the 1970s [1], it is only recently that researchers and engineers have been able to run DEM simulations of sufficiently large size and complexity

*Corresponding author: rackl@fml.mw.tum.de

to be practically useful. This has caused a rapid growth in the adoption of DEM [2], enabled by continual advances in affordable computational power. Huge numbers of studies have shown the usefulness of DEM for modelling the behavior of bulk solids in industrially relevant systems such as fluidised beds, silos, mixers or mills.

One major benefit of DEM is that the simulations require specification of a relatively small number of microstructural parameters. However, it can be difficult to establish suitable values for all of these model inputs. For example, input parameters cannot be obtained by laboratory testing for coarse-grained simulations in which the particle diameters are increased beyond their physical values to reduce the computational requirements of a simulation, e. g., [3–5]. Even if particle diameters are simulated accurately, other parameters can be difficult to relate to physical measurements, e. g., numerical damping coefficients [6] or rheological parameters required in the force–displacement laws [7]. The interparticle friction coefficient is often increased to unphysically large values in an attempt to capture particle irregularity [8]. Additional parameters which lack a physical basis are usually needed when grain crushing [9] or rolling resistance [10] are considered in the model.

When the foregoing limitations of laboratory experiments to supply model input parameters are considered, it is unsurprising that most DEM simulations contain parameters which can be obtained only by calibration. Calibration involves varying the unknown parameters until a satisfactory match has been achieved between the simulation results and the corresponding physical measurements for the response(s) of interest. Calibration is often done in an inefficient manner based on trial and error. Trial-and-error calibration has many obvious disadvantages [7]: it is not known in advance how many simulations will be needed for calibration; the success of the method depends on the modeller's experience; little, if any, mechanistic insight is gained; the calibrated parameters may be suboptimal; and using a trial-and-error approach rapidly becomes impractical as the number of parameters increases. Furthermore, DEM simulations can be very computationally expensive so running more simulations than essential for calibration is undesirable.

The significant disadvantages associated with trial-and-error calibration of DEM input parameters have motivated research into alternative approaches based on design of experiments (DoE) methods. Yoon [11] uses response surface analysis and a Plackett–Burman experimental design to identify suitable parameters to simulate uniaxial compression of bonded rock. Favier et al [12] and Johnstone [13] both use DoE methods to calibrate DEM models based on experimental measurements. Benvenuti et al. [14] train an artificial neural network for DEM simulation parameter identification. However, none of these calibration approaches are widely used in industry where *ad hoc* trial-and-error methods remain predominant.

In this paper, a novel calibration procedure is described which is based on Latin hypercube sampling and Kriging [15]. This workflow was designed to be automated, i. e., to run efficiently with minimal user intervention. It was implemented using purely open-source software including LIGGGHTS [16] and GNU Octave [17]. Both the open-source implementation and the high level of automation are intended to encourage the

widespread adoption of this calibration method. Another novel aspect is the inclusion of the simulation time-step in the calibration process. In most cases, DEM adopts an explicit, conditionally-stable time-stepping algorithm. The size of the largest time-step which maintains numerical stability is strongly dependent on the particle density and stiffness. Considering the simulation time-step during calibration means that optima requiring small time-steps to maintain stability are disfavoured. This ensures that the calibration process is prevented from converging to a solution which causes the simulation to run prohibitively slowly.

The main aim of this paper is to describe and demonstrate a novel calibration method. Spherical glass beads are used as the bulk material. Two responses are calibrated, angle of repose and bulk density, while simulation time-step is also considered during calibration. Subsidiary aims are as follows: (i) to demonstrate that significantly larger time-steps can be achieved by explicitly including the time-step as a factor in the calibration process, while still achieving an excellent match between the experimental data and the model; (ii) to show that parameter sets which differ substantially can yield similar outcomes; (iii) to explore interactions among the DEM input parameters being calibrated.

This calibration approach is generally applicable to all types of DEM simulation. The example presented in this paper is for a conventional DEM simulation in which each simulated particle represents one physical particle. However, the method has even greater potential for coarse-grained simulations for which the number of parameters requiring calibration can be very large.

2. Materials and Methods

This section contains a brief overview of DEM, followed by a more detailed description of the specific model considered in this study.

2.1. Discrete Element Method

Both hard-sphere and soft-sphere DEM simulations are possible; the latter are more frequently used and are the focus of this paper. The particle geometry is idealized to reduce the computational requirements: often spheres are used in three-dimensional simulations. The density and stiffness of each particle can differ. The particles are not permitted to deform during the simulation; instead deformation is captured by allowing the particles to overlap at contacts with surrounding particles and boundary walls. DEM is driven by a time-stepping algorithm, often a central difference, velocity–Verlet scheme. During each time-step [18], interparticle forces are evaluated at contact points based on a defined force–displacement law. This contact model is almost always based on either a linear, Hookean spring or a nonlinear, Hertzian spring along the contact normal. The interparticle contact forces are summed, along with body forces such as gravity, to calculate resultant forces for each particle. Then Newton's Second Law is applied to determine the translational and angular particle accelerations which are numerically integrated to find particle velocities

and displacements. These displacements are used to update the particle positions at the end of each time-step. Individually, these calculations are very straightforward. However, as millions of particles may be simulated using time-steps of the order of nanoseconds, the computational effort can be very considerable to simulate a short time period.

2.2. Investigated DEM Model of this Study

All simulations were run using the public version of the LIGGGHTS [16] DEM code. A Hertz–Mindlin contact model was chosen for these simulations along with an elastic–plastic spring–dashpot (EPSD) rolling friction model. This model incorporates viscous damping in its formulation [19]. The critical time-step for each simulation was computed using Equation 1 where G is the shear modulus, ρ is particle density, ν is Poisson's ratio and r is the radius of the smallest particle.

$$dt_r = \frac{\pi r \sqrt{\frac{\rho}{G}}}{0.1631\nu + 0.8766} \tag{1}$$

The time-step used for the DEM simulations was taken as a quarter of this critical Rayleigh time-step. For this paper, it is assumed that the time-step is solely a function of the parameters used in Equation 1. Although it is known that the simulation time-step must be reduced to ensure stability when particle relative velocities are large, the nature of this reduction is currently unquantified. In cases where the relative velocities are large, it is noted that the factor by which Equation 1 is multiplied (0.25) may need to be reduced to maintain stability.

The effect of this time-step on the calibration was controlled by means of a weighting factor. This weighting factor, WRL, was one of the seven factors adjusted in the calibration process. Apart from the Rayleigh time-step, two responses were calibrated: bulk density and angle of repose. The system shown schematically in Figure 1 was simulated to obtain these responses. It consists of a horizontal steel plate with a steel cylinder of diameter 100 mm resting on top so that the plate obstructs the bottom of the cylinder. A rigid ring of height 3 mm and diameter 100 mm is affixed to the steel plate to prevent particles from rolling away on the flat surface. Each simulation is run in the following manner. Particles of diameter 5 mm are poured into the cylinder under gravity ($g = 9.81\,\mathrm{m\,s^{-2}}$) to a height exceeding 50 mm and the system is allowed to settle. Any particles above 50 mm are subsequently removed from the simulation domain and the system is given time to settle again. The poured bulk density is found using the total particle mass and fill height. Then the cylinder is raised at a constant speed of $10\,\mathrm{mm\,s^{-1}}$ so that a heap is formed under the influence of gravity. After the system has settled, monochrome screenshots of the top-down perspective and side view are created. The angle of repose of the heap is found using the verified image processing algorithm described in Appendix A. The bulk density and angle of repose are compared with literature values for glass

beads: $1500\,\mathrm{kg\,m^{-3}}$ and 22°, respectively ([20, p. 16], [21]). Table 1 shows the values of the model input parameters which were fixed for all simulations.

Seven parameters were used in the calibration process: the particle density, the Young's modulus, the static friction coefficients and rolling friction coefficients between two particles and between particles and walls, and the weighting factor controlling the effect of Rayleigh time-step on the calibration (WRL). There are an infinite number of parameter sets which would satisfy the requirements for bulk density and angle of repose. By considering Rayleigh time-step, the single parameter set which maximised the time-step, and hence the efficiency of the simulation, was favored. Although particle density is often easily measured, non-physical values may be used in quasi-static simulations to increase the size of the critical time-step: so-called 'density scaling'. Furthermore, for coarse-grained simulations, the density required for the simulated particles inevitably differs from that of the physical particles so particle density usually requires calibration for coarse-grained simulations. The experimental plan which describes exactly how these parameters were varied is discussed in subsubsection 2.3.4.

2.3. Calibration Process

The calibration process described in this paper includes sampling the model to be calibrated at randomly, yet evenly, distributed points and adopting Kriging as a meta-model technique.

2.3.1. Latin Hypercube Sampling

Latin hypercube sampling was first described by McKay et al. [22]. The idea is to randomly, yet evenly, distribute samples in an N-dimensional factor domain.

Let $V_k \in [v_{k,L}; v_{k,U}]$ (where $v_{k,L} < v_{k,U}$ and $v_{k,L}, v_{k,U} \in \mathbb{R}$) be the k^{th} interval of interest of a number of factors $N \in \mathbb{N}^+$ in which $n \in \mathbb{N}^+$ sample locations are to be distributed. First of all, the domain for each V_k needs to be split into n evenly-spaced, non-overlapping subdomains $W_{k,i}$. The width w_k for each V_k's subdomain can be determined from Equation 2 and the interval of the i^{th} subdomain $W_{k,i}$ is given by Equation 3.

$$w_k = \frac{v_{k,U} - v_{k,L}}{n} \tag{2}$$

$$W_{k,i} = \begin{cases} [(i-1)w_k + v_{k,L}; \quad iw_k + v_{k,L}], & i \in [1; n-1] \\ [(n-1)w_k + v_{k,L}; \quad v_{k,U}], & i = n \end{cases} \tag{3}$$

A random value $x_{k,i}$ is drawn from each of the subdomains $W_{k,i}$. A random set is selected from the permutation of all $x_{k,i}$ such that each $W_{k,i}$ occurs once. This leads to n tuples which form an N-dimensional Latin (hyper) cube, where each tuple element is unique and the tuples are well-distributed.

In order to ensure an evenly-distributed set of tuples, the Octave package *stk* [23] created 5,000 Latin hypercube designs per included calibration factor, following the process described above. Subsequently, the distance d_c between each tuple in a respective design was computed according to the Euclidean norm (Equation 4). In Equation 4, p and q are tuples and p_j, q_j the j^{th} tuple. The distance d_c was computed for all h tuple combinations per design.

$$d_c(p,q) = \sqrt{\sum_{j=1}^{h}(p_j - q_j)^2} \tag{4}$$

d_c was used as a criterion to select the design where the minimum distance of all tuple combinations was the largest. Thus, the design selected for the sample set was the one whose minimum distance d_{sel} satisfied Equation 5 for all designs. This is called the 'MAXIMIN' criterion in the literature, e. g., [24, p.183 ff.].

$$min(d_{\text{sel}}) = max\Big(min(d_c)\Big) \tag{5}$$

2.3.2. Kriging

Kriging is a general term for a collection of statistical regression methods. There exist different modifications [25, p. 154], some of which are not clearly defined. The Kriging method used for this work is *Universal Kriging* or *Kriging with drift*. As with every regression method, the main aim is to predict values at unsampled locations from a given set of sample locations and corresponding sample response data.

The theoretical background described in this section is given in standard statistics references, e. g., [25, p. 195 ff.]. In Universal Kriging, the responses $Z_s(x_s)$ at a number, N, of sample locations x_s are considered to consist of a deterministic part $S(x_s)$ and a random part $R(x_s)$. Within the scope of this study, $S(x_s)$ in Equation 6 represents a first-order polynomial function with K coefficients β_i, which are initially not known, as well as the functions f_i. Hence, Equation 6 can be rewritten as Equation 7.

$$Z_s(x_s) = S(x_s) + R(x_s) \tag{6}$$

$$Z_s(x_s) = \sum_{i=1}^{K} \beta_i f_i(x_s) + R(x_s) \tag{7}$$

Equation 7 can be expressed for the response data of interest $\boldsymbol{Z}_u$ as in Equation 8. $\boldsymbol{Z}_u$ depends on the unsampled locations of interest $\boldsymbol{x}_u$, the design matrix $\boldsymbol{D}_{\text{lhs}}$ as obtained from Latin hypercube sampling and a vector of coefficients $\boldsymbol{\beta}$. Using an anisotropic Matérn covariance matrix [26, p. 12-14], the coefficients and weights for $\boldsymbol{\beta}$ and $R(\boldsymbol{x}_u)$ are computed by means of the restricted maximum likelihood method (ReML, [26, p. 170])). Note that the *stk* package in Octave allows for estimation of (measurement) noise from the response data, which was done for this study. By including this information, the Kriging surrogate models implicitly change their property from interpolation to approximation [27, p. 156].

$$\boldsymbol{Z}_u(\boldsymbol{x}_u) = \boldsymbol{D}_{\mathrm{lhs}}\boldsymbol{\beta} + R(\boldsymbol{x}_u) \tag{8}$$

2.3.3. Calibration Approach

The general calibration approach followed by a human calibrator is as follows. Initially, DEM models have to be created which represent physical measurement setups. These models are needed to generate the desired response(s). In the next step, the material and contact law parameters to be used for calibration are selected. Typically, the calibrator wishes to minimize the number of calibration parameters, since each additional parameter increases the complexity of the calibration task. After this, material parameters with which to start the calibration are either measured or taken from literature. Very often, only parameter ranges are available, as there is always some form of variation in the measurement data. Once the parameters have been chosen and set, the DEM models are sampled using different parameter sets to gain insight into which parameter or combination of parameters influences the responses. As soon as the relationship between calibration parameters and response values has been established, the values of the calibration parameters are adjusted until the responses match the experimental values within a desired tolerance, e. g., standard error of the measurement. It is obvious that the sampling process as well as parameter adaptation are highly repetitive tasks which involve a lot of data handling. Thus, these steps were chosen to be automatized. Using Latin hypercube sampling and Kriging, the main aim was to develop a versatile and robust calibration process.

In order to convert the widely-used trial-and-error approach for DEM material parameter calibration into a method suitable for automatization, three presumptions were made. (i) If no parameter value is available or it varies with different bulk solid batches, the person calibrating will be likely to find this parameter to lie within an interval, rather than being a constant value. This is often the case for friction values, which are influenced by many micromechanical factors, for example. Furthermore, when physical measurements are unavailable or difficult to obtain, the calibrator will find a range of values in the literature. Uncertainty in the order of magnitude of a parameter can be reflected by increasing the interval width. Nonetheless, increasing it for the particle density or Young's modulus has to be done carefully since both also influence the Rayleigh time-step. Excessively wide intervals for either of these parameters could impose excessive weight on the Rayleigh time-step during the calibration [28]. (ii) Incorporating more experimental data for the calibration will increase the validity of the calibrated DEM parameter set. The calibration procedure is therefore designed to work with several DEM models and responses simultaneously. (iii) A human calibrator is incapable of efficiently capturing effects of a single factor and the interactions at the same time, particularly if there are several responses. However, this is the most important prerequisite when working with multivariate data and the key to reducing the number of calibration runs to a minimum. As a consequence, the task of keeping track of effects and predicting the results of parameter changes is carried

out by means of a meta-model (Kriging) in combination with suitable sampling (Latin hypercube) as well as numerical optimization.

Figure 2 outlines the workflow of the three phases of the calibration process. After the calibration parameters and their respective intervals are set by the user, the process requires no further user intervention. It starts by generating a set of sample parameter sets based on Latin hypercube sampling, forwards them to the DEM models and collects the response data (sampling phase). In the next step, the Kriging meta-models are parameterized with the sample parameter sets and corresponding responses. Using these meta-models, an optimization process is initiated (1^{st} optimization phase). The starting value of the optimization is the mean value of each parameter interval. The idea is to use the computationally cheap meta-models to identify a promising starting value for the DEM optimization step which is far more computationally expensive. Finally, the optimal parameter set from the meta-models is used as starting value for the optimization with the actual DEM models (2^{nd} optimization phase). This is to verify the prediction from Kriging and refine the quantitative calibration outcome.

For a conventional DEM simulation without coarse graining, it is possible that the number of parameters requiring calibration may be very small. For cases with only one or two unknown parameter values, the development of Kriging meta-models is unnecessarily expensive. This calibration method requires a larger set of unknown parameters in order to be viable.

Optimization was carried out using the multi-objective Levenberg-Marquardt residual minimization algorithm [29, 30], as implemented in the GNU Octave package *optim* [31]. The optimization was set to terminate when the improvement in the objective function was less than 2 % between two iterations. The reason for this was to avoid a large number of optimization steps, of which the last ones would only improve the absolute calibration outcome marginally. The maximum absolute tolerance between the desired values and the calibrated responses should be specified by the calibrator; because bulk solid measurements can feature scatter of several percent, it would be unnecessary and wasteful to calibrate the model parameters meticulously.

The same multi-objective cost functions are used for both optimization steps. Response values are taken into account using Equation 9, where s_i is the DEM response and m_i (> 0) is the corresponding desired experimental value.

$$c_i = \frac{s_i - m_i}{m_i} \tag{9}$$

With regard to computational efficiency of the calibrated DEM parameter set, a large value of the Rayleigh time-step size is desired. However, unlike angle of repose or bulk density, there exists no globally optimal Rayleigh time-step size since Equation 1 is unrestricted in its maximum value. The cost function used in this study hence seeks to obtain the largest possible value with regard to the initially specified parameter intervals. It is shown in Equation 10, where r_{max} and r_{min} are the maximum and minimum

possible Rayleigh time-steps, respectively, dt_r is the Rayleigh time-step of the current parameter set and WRL is a weighting factor, subject to investigation in this study. The authors are unaware of any prior studies where the Rayleigh time-step size was actively considered as a calibration target.

$$t_i = WRL \cdot \frac{r_{max} - dt_r}{r_{max} - r_{min}} \tag{10}$$

The approach described above is generally applicable. The specific example used to demonstrate its usefulness contains seven unknown parameter values as described in subsection 2.2. The experimental plan for this specific case is given in subsubsection 2.3.4 and the results are presented and discussed in section 3.

2.3.4. Experimental Plan for Numerical Experiments

The experimental plan of this study is listed in Table B-1 in the appendix. It was created using the Design of Experiments (DoE) package RcmdrPlugin.DoE [32], of the statistical programming software R [33]. The Design of Experiments comprises four factors on two levels and two factors on three levels and is based on an orthogonal array (L72.2.56.3.2 in RcmdrPlugin.DoE), which was optimized for a minimum of three- and four-factor interactions. The numbers of generalized words of lengths 3, 4 and 5, as returned by R, are 0.00, 0.27 and 0.49, respectively. Consequently, reducing the number of experiments to 72, as compared to 144 in a full-factorial design, resulted in a well-balanced experimental plan with only slight confounding.

The factors and their respective levels are listed below. For the four factors on two levels, the levels were 0 and 1, which indicate if the respective parameter was included for calibration (1) or not (0).

WRL weighting factor for the Rayleigh time-step within Equation 10; $\in [0, 0.5, 1]$.

SPP number of Latin hypercube samples per calibration parameter; note that particle density and particle to particle rolling friction were always included for calibration; $\in [3, 6, 9]$.

MU_PP static friction between particle and particle: 0 or 1.

MU_PW static friction between particle and wall: 0 or 1.

YM Young's modulus: 0 or 1.

RF_PW rolling friction between particle and wall: 0 or 1.

The number of sample locations was determined according to Equation 11, where S is the number of sample locations generated by the Latin hypercube sampling algorithm, f_{cal} is the number of DoE factors included in the calibration and SPP is the factor from the experimental plan. Note the specification of $(f_{\text{cal}} + 2)$ in Equation 11: particle density and the rolling friction between particles (RF_PP) were always included for calibration and are therefore omitted from the experimental plan shown in Table B-1.

$$S = (f_{\text{cal}} + 2) \cdot SPP \tag{11}$$

If a parameter were used for calibration, its value interval was selected from the pre-defined list in Table 2. These intervals were defined by the authors according to published data from experiments and DEM simulations with glass beads [34–52]. Recalling subsubsection 2.3.3, this is a typical situation where data from literature are ambiguous and the calibrator knows an approximate range for most of the calibration parameters. In order to speed up the computations, the Young's modulus found in literature was scaled down by two orders of magnitude; it was found in preliminary simulations that the results for the angle of repose and the bulk density are unaffected by this which agrees with published findings [53]. When a parameter was excluded from calibration, its value was set constant. These values were MU_PP=0.2, MU_PW=0.2, RF_PW=0.01, YM=5.06×10^8 Pa.

For each of the single runs specified in the experimental plan in Table B-1, a full calibration process as described in subsubsection 2.3.3 was set up and run on a computer with 12 CPUs. The calibration script was given the desired values for the bulk density and angle of repose, as well as the respective calibration parameter intervals. The calibration process then took place without any user intervention. The overall computation time was approximately 350 hours for all 72 runs.

3. Results and Discussion

In general, the calibration procedure worked reliably and led to satisfactory calibration outcomes. Various correlations and the effect of the Rayleigh time-step were investigated.

3.1. General Findings Related to the Calibration Process

For all cases both the Kriging and DEM optimization were terminated due to the improvement in the objective function being less than specified.

The absolute difference between desired and calibrated angle of repose and bulk density for all of the 72 experiments are depicted in the boxplots in Figure 3. It can be seen that especially the bulk density was calibrated very precisely. The angle of repose outcome shows a greater scatter; however at least 75 % of the runs led to an angle of repose value which was within a maximum tolerance of around 15 % of the desired value of 22°. To some extent, this greater scatter can be explained by the angle of repose being somewhat hard to reproduce in simulations as well as physical experiments. The relative differences of the bulk density and angle of repose are similar in magnitude to those which can be expected from physical measurements.

These values for the angle of repose and bulk density were obtained by a wide variety of parameter sets. Figure 4 depicts a boxplot for each parameter used in the calibration. Values of the particle density and Young's modulus tend to lie at the upper and lower ends of their corresponding intervals, respectively.

This is likely due to the influence of the optimization criterion of the Rayleigh time-step, which favors high particle density and low Young's modulus values to obtain a large time-step (cf. Equation 1). The static and rolling friction values between particle and wall (MU_PW, RF_PW) are spread out over almost the entirety of their interval. This indicates that their effect on the calibration process is negligible.

The material model and contact law parameters of the Kriging models and the DEM model show almost perfect correlation. Relevant correlation coefficients are listed in Table 3. This means that the Kriging meta-models were able to predict the optimal parameters precisely. Table 4 lists the correlation coefficients between DEM and Kriging for the angle of repose, bulk density and Rayleigh time-step. Bulk density and Rayleigh time-step agree very well, while the correlation between the angle of repose responses is much lower at 0.72. This underlines the poor reproducibility of the angle of repose. Overall, the Kriging functions were able to predict calibration parameter values and calibration target responses reliably and accurately.

3.2. Multivariate Analysis of Variance Results

Using the six calibration parameters as factors and the angle of repose, bulk density and Rayleigh time-step as responses, a multivariate analysis of variance (MANOVA) was carried out. The underlying model took into account primary factors as well as two-factor interactions. The variance was analyzed for the Kriging as well as the DEM data and results are listed in Table 5, where a colon between two factors denotes their two-factor interaction. The Kriging meta-models show significant effects for all of the single factors at the $\alpha = 0.05$ level, but none of the two-factor interactions. This is the main difference compared to the DEM model, where the two-factor interactions DENS:MU_PP, DENS:RF_PP, DENS:YM and MU_PP:RF_PP were also found to be significant while MU_PW was not. These MANOVA results again confirm that the Kriging meta-models are a suitable means to predict the behavior of the DEM model. Nonetheless, the second optimization process, which uses the actual DEM model, is still required to refine the calibration outcome.

3.3. Correlations between Friction Parameters used for Calibration

Friction values for different pairs of materials are often set equal (e. g., [35, 38]), i. e., setting the values for MU_PP equal to those for MU_PW. This may be due to two reasons. Measured values could be unavailable or have no physical analogue in the case of rolling friction. Alternatively, it could be an attempt to reduce the number of calibration parameters and, thus, decrease the complexity of the calibration process, since satisfactorily calibrating many parameters is difficult with trial-and-error methods. Table 6 shows the Pearson correlation coefficients between static and rolling friction coefficients of the DEM model. The largest magnitude of correlation by far was found between MU_PP and RF_PP at -0.659, while all other correlation coefficients were negligible (< 0.25). This indicates that there is no sensible justification for setting particle–particle and particle–wall friction coefficients equal to each other and that calibration is required for each single friction value.

3.4. Effect of the Rayleigh Time-step Cost Function

This study is the first to actively include the Rayleigh time-step size as a calibration criterion for DEM material model calibration. Figure 5 depicts the effect of the weighting factor, WRL, on the Rayleigh time-step, angle of repose and bulk density. Including the Rayleigh time-step in the optimization (WRL=0.5 or 1) leads to a significantly larger time-step. This is beneficial for further application of the calibrated parameter set, as fewer time-steps will be required to simulate processes of any fixed duration. While the Rayleigh time-step is considerably larger, the angle of repose calibration outcome is not significantly affected. The bulk density is largely influenced by the particle density, so as the weighting factor of the Rayleigh time-step increases, the bulk density similarly increases. This is in agreement with the findings reported by Rackl et al. [28].

Nevertheless, the absolute difference between WRL=0 and WRL=1 is only a few percent for the bulk density. Only two of the specified parameters in Table 2, particle density (DENS) and Young's modulus (YM), affect the Rayleigh time-step. Since the YM significantly influences neither the bulk density nor the angle of repose (cf. second to last paragraph in subsubsection 2.3.4), its value will thus always tend to favor a large Rayleigh time-step due to the cost function specified in this work. This is supported by the value range for the YM in Figure 4, which clearly shows that the YM was consistently chosen at the lower end of its interval. Thus, the only effective parameter to increase the Rayleigh time-step is DENS which has a much smaller effect on the time-step. The absolute effect of the Rayleigh-related part of the cost function on the Rayleigh time-step would presumably be more dominant if stiffness-related measurement data were to be calibrated and a compromise between stiffness and Rayleigh time-step had to be found.

3.5. Efficiency of the Calibration Process

The efficiency of the overall calibration process can be assessed from the number of times the DEM model has to be run. DEM models are typically computationally expensive; to save time during the calibration process, it is desired to achieve the calibration aims with the smallest number of runs possible. In the calibration process described in this study, the number of overall DEM model runs can be expressed as a sum of two phases. The first phase is related to the number of sample points of the Latin hypercube sampling and the related number of runs is known *a priori* through Equation 11. The second optimization phase of the procedure is based on the DEM model. The total number of iterations to find a satisfactory parameter set is only known after the calibration process is complete.

The number of required DEM model runs during the optimization step over the number of Latin hypercube samples per calibration parameter (SPP) is shown on the left of Figure 6. This number varies between approximately 10 and 55. It somewhat decreases with more initial samples for WRL=0 and WRL=0.5 and its dependency on the Rayleigh time-step weighting factor (WRL) cannot be estimated from the present results. In theory, the Kriging meta-models will be able to yield more precise predictions if more samples

were used to parametrize them. Hence the number of required optimization runs should decrease as the number of samples increases, which is supported by the findings for WRL=0 and WRL=0.5. However, the results for WRL=1 do not show this trend.

On the right side of Figure 6, the overall number of DEM model runs is depicted. This equals the sum of sampling runs and optimization runs and it increases with more initial samples. Thus, even though the number of required optimization runs decreases with an increased number of samples, this effect is not large enough to compensate for the increased number of initial sampling runs. Since the smallest amount of overall runs is obtained from only three samples per parameter, the authors suggest using this value for the described workflow in the future.

The described calibration procedure required an average of 51 DEM model runs to finish, where all required steps were performed automatically. With an average runtime of six minutes per run, it therefore took about 5 hours to identify a set of parameters.

Figure 7 shows the influence of SPP on the calibration outcome of the angle of repose and bulk density. There is no significant effect of SPP on the precision of the calibration results. However, this may change if SPP is reduced below some unknown critical value which depends on the DEM model.

4. Conclusions

The main aim of this study was to demonstrate the usefulness of a novel calibration method for DEM material model parameters, based on angle of repose and bulk density tests. Various parameter combinations were tested in a design of experiments in order to assess the influence of the number of initial samples, to evaluate the influence of considering the time-step within the optimization process and to explore interactions among the DEM parameters.

The calibration method yielded a satisfactory outcome for the angle of repose and bulk density, comparing with the target values. Moreover, the outcome can be considered very good when taking into account the typical experimental scatter for the bulk density (approx. 5–10 %) and the angle of repose ($\pm$ 1°–2°).

When the Rayleigh time-step was included in the calibration, the time-step increased significantly, while the target values of the angle of repose and bulk density were still achieved satisfactorily. This is important to obtain efficient DEM parameter sets because, for a process with a fixed duration, each increase of the critical Rayleigh time-step size correspondingly reduces the number of overall required iterations and hence the computational time.

No correlation was found among the friction coefficients. Hence setting pairs of these coefficients to the same value for the sake of decreasing the parameter count lacks justification, at least with regard to the angle of repose and bulk density.

The results from this paper reveal that there exists a solution space of feasible DEM parameter sets

which lead to similar results for the desired calibration targets (angle of repose, bulk density). It was demonstrated by Rackl et al. [28] that including more target values reduces the variety of parameter sets of such a solution space. It should be clarified that in order to represent the physical behavior of a bulk solid, appropriate and sufficient experimental data are required. Calibration should be carried out based on as many physical experiments as possible. Considering six or more parameters, as done in this study, renders the often used trial-and-error approach highly inefficient and highlights the need for systematic and automatized calibration methods.

Further research should focus on two major aims. The first aim would be to add more DEM models to the calibration procedure, e. g., a shear cell or triaxial compression test, and study the effect on the calibration outcome. Adding more DEM models and corresponding measurement results to the calibration process will enable the calibrated DEM parameter set to be employed for a wider range of applications. If, for example, the stiffness behavior is of importance, then a uniaxial compression test might be added. It shall be noted that calibration is only sensible if the laboratory tests are somewhat representative of the foreseen application to be simulated. As a second aim, the number of required calibration runs of the DEM models should be minimized. Apart from the number of initial Latin hypercube samples, there are parameters which have not been taken into account in this study. For example, the optimization algorithm could be altered, since numerous DEM model runs can be attributed to gradient computation of the Levenberg-Marquardt scheme. Another option is to take the measurement error from the bulk material experiments into account and adapt the tolerance settings of the optimization algorithm accordingly; for example, there is no need to calibrate the angle of repose as precisely as a few percent if the experimental scatter is $\pm 10\,\%$.

Availability of the Calibration Procedure Scripts

The GNU Octave scripts used in this study are scheduled to be released as open-source code after AiF project no. 18371 N/1 ends in spring 2017.

Conflict of Interest

There is no conflict of interest.

Acknowledgment

This study received funding by the AiF (no. 18371 N/1), within the program for sponsorship by Industrial Joint Research (IGF) of the German Federal Ministry of Economic Affairs and Energy based on an enactment of the German Parliament.

References

[1] P. A. Cundall, O. D. L. Strack, A discrete numerical model for granular assemblies, Géotechnique 29 (1) (1979) 47–65. doi:10.1680/geot.1979.29.1.47.

[2] H. P. Zhu, Z. Y. Zhou, R. Y. Yang, A. B. Yu, Discrete particle simulation of particulate systems: Theoretical developments, Chem. Eng. Sci. 62 (13) (2007) 3378–3396. doi:10.1016/j.ces.2006.12.089.

[3] M. Sakai, S. Koshizuka, Large-scale discrete element modeling in pneumatic conveying, Chem. Eng. Sci. 64 (3) (2009) 533–539. doi:10.1016/j.ces.2008.10.003.

[4] M. Sakai, M. Abe, Y. Shigeto, S. Mizutani, H. Takahashi, A. Viré, J. R. Percival, J. Xiang, C. C. Pain, Verification and validation of a coarse grain model of the DEM in a bubbling fluidized bed, Chem. Eng. J. 244 (2014) 33–43. doi:10.1016/j.cej.2014.01.029.

[5] D. S. Nasato, C. Goniva, S. Pirker, C. Kloss, Coarse graining for large-scale DEM simulations of particle flow – an investigation on contact and cohesion models, Procedia Eng. 102 (2015) 1484–1490. doi:10.1016/j.proeng.2015.01.282.

[6] D. O. Potyondy, P. A. Cundall, A bonded-particle model for rock, Int. J. Rock Mech. Min. 41 (8) (2004) 1329–1364. doi:10.1016/j.ijrmms.2004.09.011.

[7] K. J. Hanley, C. O'Sullivan, J. C. Oliveira, K. Cronin, E. P. Byrne, Application of Taguchi methods to DEM calibration of bonded agglomerates, Powder Technol. 210 (3) (2011) 230–240. doi:10.1016/j.powtec.2011.03.023.

[8] X. Huang, K. J. Hanley, C. O'Sullivan, C.-Y. Kwok, Exploring the influence of interparticle friction on critical state behaviour using DEM, Int. J. Numer. Anal. Met. 38 (12) (2014) 1276–1297. doi:10.1002/nag.2259.

[9] K. J. Hanley, C. O'Sullivan, X. Huang, Particle-scale mechanics of sand crushing in compression and shearing using DEM, Soils Found. 55 (5) (2015) 1100–1112. doi:10.1016/j.sandf.2015.09.011.

[10] J. Ai, J. F. Chen, J. M. Rotter, J. Y. Ooi, Assessment of rolling resistance models in discrete element simulations, Powder Technol. 206 (3) (2011) 269–282. doi:10.1016/j.powtec.2010.09.030.

[11] J. Yoon, Application of experimental design and optimization to PFC model calibration in uniaxial compression simulation, Int. J. Rock Mech. Min. 44 (6) (2007) 871–889. doi:10.1016/j.ijrmms.2007.01.004.

[12] J. Favier, D. Curry, R. LaRoche, Calibration of DEM material models to approximate bulk particle characteristics, in: Proc. 6$^{\text{th}}$ World Congress on Particle Technology, Nuremberg, Germany, 2010.

[13] M. Johnstone, Calibration of DEM models for granular materials using bulk physical tests, Ph.D. thesis, The University of Edinburgh (2010).

[14] L. Benvenuti, C. Kloss, S. Pirker, Identification of DEM simulation parameters by Artificial Neural Networks and bulk experiments, Powder Technol. 291 (2016) 456–465. doi:10.1016/j.powtec.2016.01.003.

[15] M. Rackl, C. D. Görnig, K. J. Hanley, W. A. Günthner, Efficient calibration of discrete element material model parameters using Latin hypercube sampling and Kriging, in: M. Papadrakakis, V. Papadopoulos, G. Stefanou, V. Plevris (Eds.), ECCOMAS Congress 2016 – Proceedings of the VII European Congress on Computational Methods, Vol. II, Crete Island, Greece, 2016, pp. 4061–4072.

[16] C. Kloss, C. Goniva, A. Hager, S. Amberger, S. Pirker, Models, algorithms and validation for opensource DEM and CFD–DEM, Prog. Comput. Fluid Dyn. 12 (2/3) (2012) 140–152. doi:10.1504/PCFD.2012.047457.

[17] J. W. Eaton, D. Bateman, S. Hauberg, R. Wehbring, GNU Octave version 4.0.0 manual: a high-level interactive language for numerical computations (2015).

[18] C. O'Sullivan, Particulate discrete element modelling: A geomechanics perspective, 1st Edition, Taylor & Francis, Oxford, UK, 2011.

[19] DCS Computing GmbH, gran rolling_friction epsd model (2016).
URL http://www.cfdem.com/media/DEM/docu/gran_rolling_friction_epsd.html

[20] R. L. Brown, J. C. Richards, P. V. Danckwerts, Principles of Powder Mechanics: Essays on the Packing and Flow of Powders

and Bulk Solids, Vol. 10 of International series of monographs in chemical engineering, Elsevier Science, Burlington, VT, US, 1970.

[21] A. C.-Y. Wong, Characterisation of the flowability of glass beads by bulk densities ratio, Chem. Eng. Sci. 55 (18) (2000) 3855–3859. doi:10.1016/S0009-2509(00)00048-8.

[22] M. D. McKay, R. J. Beckman, W. J. Conover, A comparison of three methods for selecting values of input variables in the analysis of output from a computer code, Technometrics 21 (2) (1979) 239. doi:10.2307/1268522.

[23] J. Bect, E. Vazquez, STK: a Small (Matlab/Octave) Toolbox for Kriging. Release 2.3, 2014.
URL http://kriging.sourceforge.net

[24] T. J. Santner, B. J. Williams, W. I. Notz, The Design and Analysis of Computer Experiments, Springer Series in Statistics, Springer, New York, NY, 2003. doi:10.1007/978-1-4757-3799-8.
URL http://dx.doi.org/10.1007/978-1-4757-3799-8

[25] R. Webster, M. A. Oliver, Geostatistics for environmental scientists, 2nd Edition, Statistics in practice, Wiley, Chichester, 2007.

[26] M. L. Stein, Interpolation of Spatial Data: Some Theory for Kriging, Springer Series in Statistics, Springer, New York, NY, 1999. doi:10.1007/978-1-4612-1494-6.
URL http://dx.doi.org/10.1007/978-1-4612-1494-6

[27] J. P. Kleijnen, Design and Analysis of Simulation Experiments, Vol. 111 of International Series in Operations Research & Management Science, Springer Science+Business Media LLC, Boston, MA, 2008. doi:10.1007/978-0-387-71813-2.
URL http://dx.doi.org/10.1007/978-0-387-71813-2

[28] M. Rackl, K. J. Hanley, W. A. Günthner, Verfication of an automated work flow for discrete element material parameter calibration, in: X. Li, Y. Feng, G. Mustoe (Eds.), Proceedings of the 7th International Conference on Discrete Element Methods, Springer Proceedings in Physics, Springer Singapore, Singapore, 2016, p. in press.

[29] K. Levenberg, A method for the solution of certain non-linear problems in least squares, Q. Appl. Math. 2 (2) (1944) 164–168.
URL http://www.jstor.org/stable/43633451?seq=1#page_scan_tab_contents

[30] D. W. Marquardt, An algorithm for least-squares estimation of nonlinear parameters, J. Soc. Ind. Appl. Math. 11 (2) (1963) 431–441. doi:10.1137/0111030.

[31] O. Till, optim: Non-linear optimization toolkit. release 1.5.0 (2016).
URL http://octave.sourceforge.net/optim/

[32] U. Groemping, RcmdrPlugin.DoE: R Commander Plugin for (industrial) Design of Experiments (2014).
URL http://CRAN.R-project.org/package=RcmdrPlugin.DoE

[33] R Core Team, R: A Language and Environment for Statistical Computing (2014).
URL http://www.R-project.org/

[34] A. Aigner, S. Schneiderbauer, C. Kloss, S. Pirker, Determining the coefficient of friction by shear tester simulation, in: M. Bischoff, E. Onate, D. Owen, E. Ramm, P. Wriggers (Eds.), Proc. 3rd International Conference on Particle-Based Methods (Particles 2013), International Center for Numerical Methods in Engineering (CIMNE), Barcelona, 2013, pp. 335–342.

[35] R. Bharadwaj, W. R. Ketterhagen, B. C. Hancock, Discrete element simulation study of a Freeman powder rheometer, Chem. Eng. Sci. 65 (21) (2010) 5747–5756. doi:10.1016/j.ces.2010.04.002.

[36] I. Cavarretta, C. O'Sullivan, E. Ibraim, M. Lings, S. Hamlin, D. M. Wood, Characterization of artificial spherical particles for DEM validation studies, Particuology 10 (2) (2012) 209–220. doi:10.1016/j.partic.2011.10.007.

[37] Y.-C. Chung, J. Y. Ooi, Experimental measurement and discrete element modelling of a dense granular medium under loading, in: Proc. Joint MSME/ASCE/SES Conference on Mechanics and Materials, Louisiana, USA, 2005.

[38] Y.-C. Chung, J. Y. Ooi, Confined compression and rod penetration of a dense granular medium: discrete element modelling and validation, in: W. Wu, H.-S. Yu (Eds.), Modern Trends in Geomechanics, Vol. 106 of Springer Proceedings in Physics, Springer-Verlag Berlin Heidelberg, Berlin, Heidelberg, 2006.

[39] Y.-C. Chung, J. Y. Ooi, A study of influence of gravity on bulk behaviour of particulate solid, Particuology 6 (6) (2008) 467–474. doi:10.1016/j.partic.2008.07.017.

[40] J. Dove, D. Bents, J. Wang, B. Gao, Particle-scale surface interactions of non-dilative interface systems, Geotext. Geomembranes 24 (3) (2006) 156–168. doi:10.1016/j.geotexmem.2006.01.002.

[41] J. Fleischmann, R. Serban, D. Negrut, P. Jayakumar, On the importance of displacement history in soft-body contact models, J. Comput. Nonlinear Dyn. 11 (4) (2016) 044502. doi:10.1115/1.4031197.

[42] S. F. Foerster, M. Y. Louge, H. Chang, K. Allia, Measurements of the collision properties of small spheres, Phys. Fluids 6 (3) (1994) 1108. doi:10.1063/1.868282.

[43] P. Gondret, M. Lance, L. Petit, Bouncing motion of spherical particles in fluids, Phys. Fluids 14 (2) (2002) 643–652. doi:10.1063/1.1427920.

[44] J. Härtl, J. Y. Ooi, Experiments and simulations of direct shear tests: Porosity, contact friction and bulk friction, Granul. Matter 10 (4) (2008) 263–271. doi:10.1007/s10035-008-0085-3.

[45] J. Havlica, K. Jirounkova, T. Travnickova, M. Kohout, The effect of rotational speed on granular flow in a vertical bladed mixer, Powder Technol. 280 (2015) 180–190. doi:10.1016/j.powtec.2015.04.035.

[46] M. Kheiripour Langroudi, J. Sun, S. Sundaresan, G. I. Tardos, Transmission of stresses in static and sheared granular beds: The influence of particle size, shearing rate, layer thickness and sensor size, Powder Technol. 203 (1) (2010) 23–32. doi:10.1016/j.powtec.2010.03.028.

[47] Y. Li, Y. Xu, S. Jiang, DEM simulations and experiments of pebble flow with monosized spheres, Powder Technol. 193 (3) (2009) 312–318. doi:10.1016/j.powtec.2009.03.009.

[48] Y. Li, Y. Xu, C. Thornton, A comparison of discrete element simulations and experiments for 'sandpiles' composed of spherical particles, Powder Technol. 160 (3) (2005) 219–228. doi:10.1016/j.powtec.2005.09.002.

[49] J. O'Donovan, G. Marketos, C. O'Sullivan, Novel methods for bender element test analysis, in: K. Soga, K. Kumar, G. Biscontin, M. Kuo (Eds.), Geomechanics from micro to macro, CRC Press/Balkema, Leiden, The Netherlands, 2015, pp. 311–316.

[50] M. Otsubo, C. O'Sullivan, W. W. Sim, E. Ibraim, Quantitative assessment of the influence of surface roughness on soil stiffness, Géotechnique 65 (8) (2015) 694–700. doi:10.1680/geot.14.T.028.

[51] S. Yang, K. Luo, M. Fang, K. Zhang, J. Fan, Three-dimensional modeling of gas–solid motion in a slot-rectangular spouted bed with the parallel framework of the Computational Fluid Dynamics–Discrete Element Method coupling approach, Ind. Eng. Chem. Res. 52 (36) (2013) 13222–13231. doi:10.1021/ie401811y.

[52] Y. C. Zhou, B. H. Xu, A. B. Yu, P. Zulli, An experimental and numerical study of the angle of repose of coarse spheres, Powder Technol. 125 (1) (2002) 45–54. doi:10.1016/S0032-5910(01)00520-4.

[53] S. Lommen, D. Schott, G. Lodewijks, DEM speedup: Stiffness effects on behavior of bulk material, Particuology 12 (2014) 107–112. doi:10.1016/j.partic.2013.03.006.

[54] C. Draug, image 2.4.1 (package for GNU Octave).
URL http://octave.sourceforge.net/image/

[55] European Federation of Materials Handling, FEM 2.582: General properties of bulk materials and their symbolization (November 1991).

Appendix A. Angle of Repose Measurement using Image Processing

As shown in Figure 8, the angle of repose α is generally defined as the angle between the horizontal and the lateral surface of a heap formed under gravity. The basic assumption from continuum theory is that the shape of the heap resembles a cone.

The following prerequisites were necessary to carry out the automatized angle of repose measurements in this study. A sphere of 50 mm diameter was added as a reference to the simulation result of a settled heap, such that it did not intersect with the heap. Two high-resolution bitmap graphics were created from LIGGGHTS, one showing the heap in a top-down view (Figure 9a) and the other in a side view (Figure 9b). For ease of the image processing, the colors were set to black for particles and white for the background; neither the cylindrical container nor the bottom plate were exported into these graphics. The Octave package *image* [54] was used for image processing.

For measuring the angle of repose, the approach described in an FEM standard [55] was adapted. In this standard, the angle of repose is determined based on the heap's diameter and height. Thus, the image processing workflow was divided into two parts. Firstly, the heap's diameter was determined as follows:

1. Read in the top-down view, e. g., Figure 9a.
2. Detect the two largest objects (which are the sphere and the heap) and remove any other objects.
3. Compute the length scale per pixel based in the occupied surface projection of the sphere (a circle) and its known diameter; remove the sphere.
4. Obtain the area of all black pixels left on the image A_t (which is only the heap), compute the center of this area and use this as the center for a circle with radius $r_l = \sqrt{A_t/\pi}$
5. Remove any black pixels outside of this circle.
6. Repeat steps 4 and 5 once and obtain an updated radius r_t. This is done in order to reduce the circle's diameter, because the outer area of the heap is less densely packed with particles, as can be seen from Figure 9a.
7. Using the length scale from step 3, the radius r_t is converted to millimeters. This new radius r_f is considered the diameter of the heap.

Determination of the height of the heap was carried out using the steps described below:

1. Read in the side view, e. g., Figure 9b.
2. Detect the two largest objects (which are the sphere and the heap) and remove any other objects.
3. Compute the length scale per pixel based in the occupied surface projection of the sphere (a circle) and its known diameter; remove the sphere.
4. Within the image matrix, find the first and last row holding a black pixel. The difference of these row numbers h_t equals the heap's height in pixel units.

5. Using the length scale from step 3, the height h_t is converted into millimeters, renamed h_f, and considered the height of the heap.
6. To account for the bottom layer of spheres, which were obstructed by the ring around the bottom plate, 5 mm (particle diameter) were subtracted from h_f in this study.

Finally, the angle of repose α was computed according to Equation A.1.

$$\alpha = \arctan \frac{h_f}{r_f} \tag{A.1}$$

Appendix B. Experimental Plan

The experimental plan of this study is listed in Table B-1.

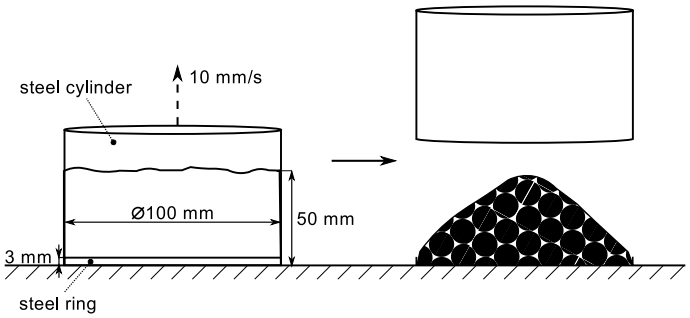

Figure 1: Schematic of the three-dimensional simulated system used to measure bulk density and angle of repose.

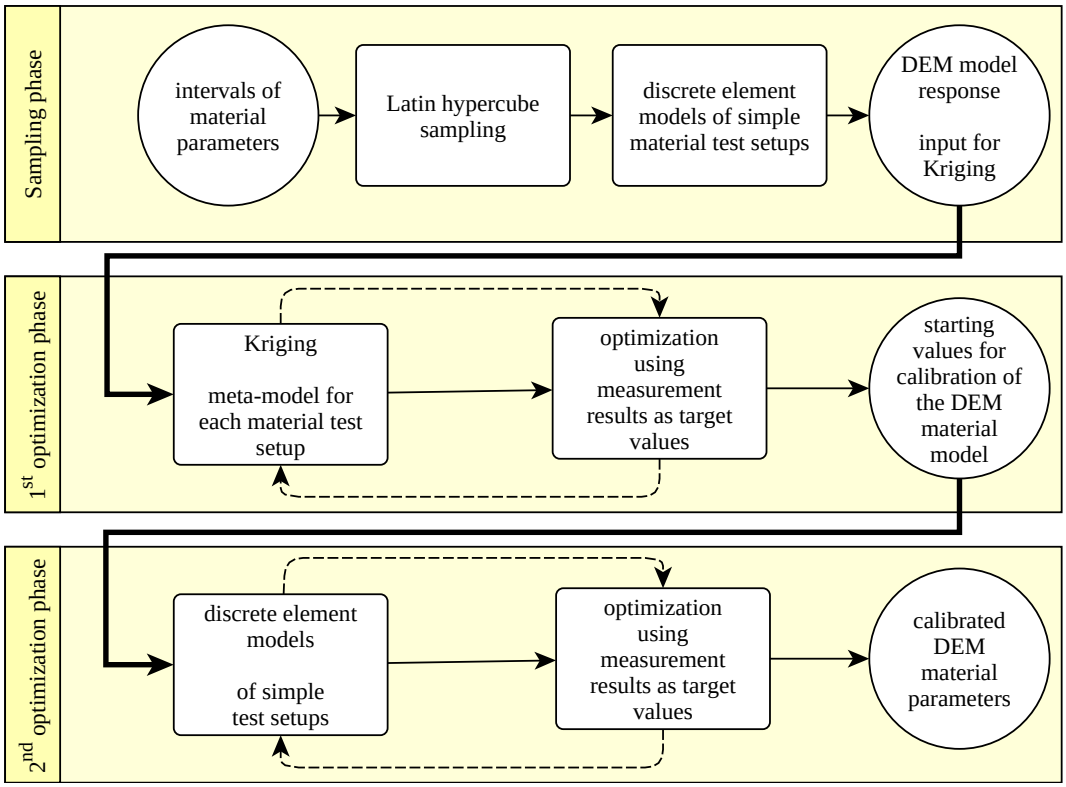

Figure 2: Workflow of the calibration process (adapted from [15]).

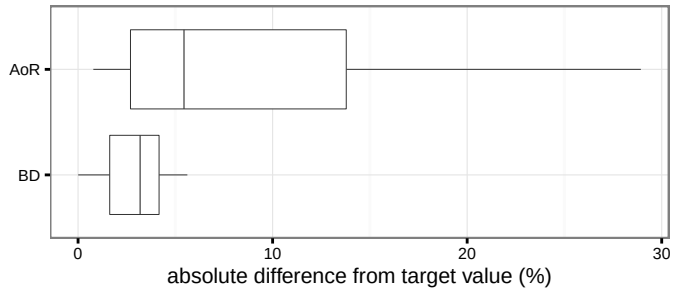

Figure 3: Boxplots of the absolute differences between the desired and calibrated angle of repose (AoR) and bulk density (BD).

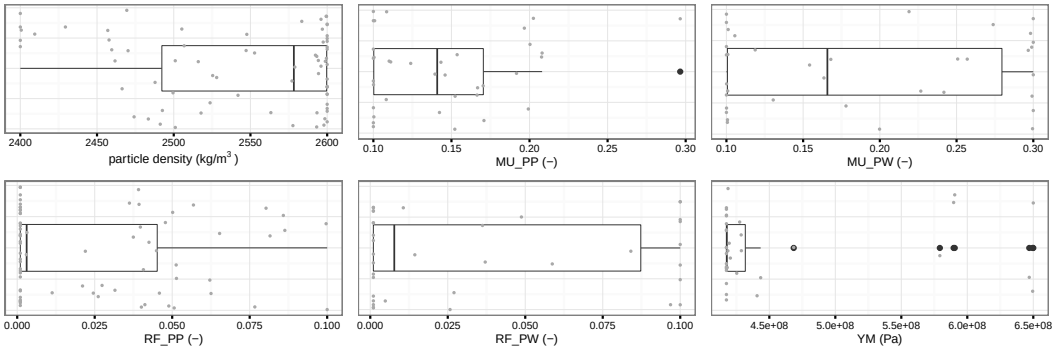

Figure 4: Boxplots for all calibrated parameters. Outliers are depicted as large black dots, while small gray dots represent the actual values.

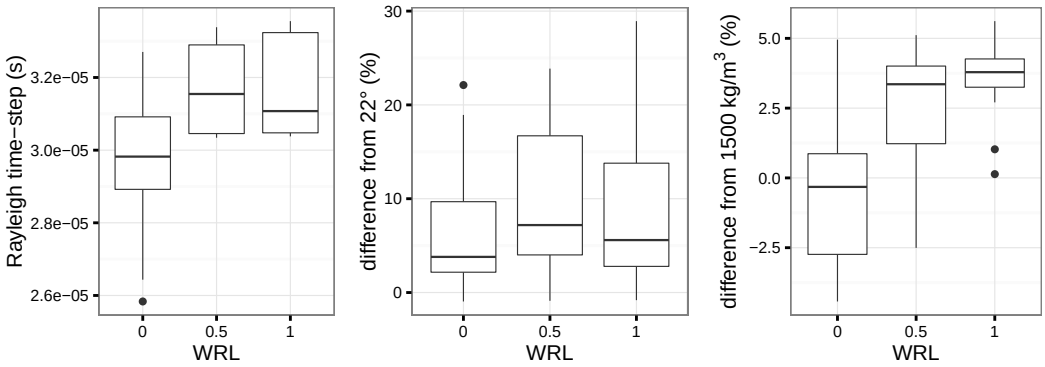

Figure 5: Boxplots showing the effect of the weighting factor of the Rayleigh time-step cost function on the Rayleigh time-step (left), angle of repose (middle) and bulk density (right).

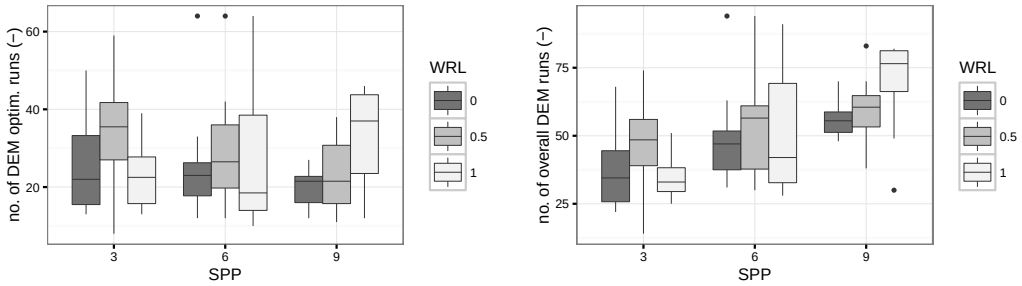

Figure 6: Number of required DEM model optimization runs (left) and overall DEM model runs (right) over the number of samples per parameter (SPP), depicted as boxplots.

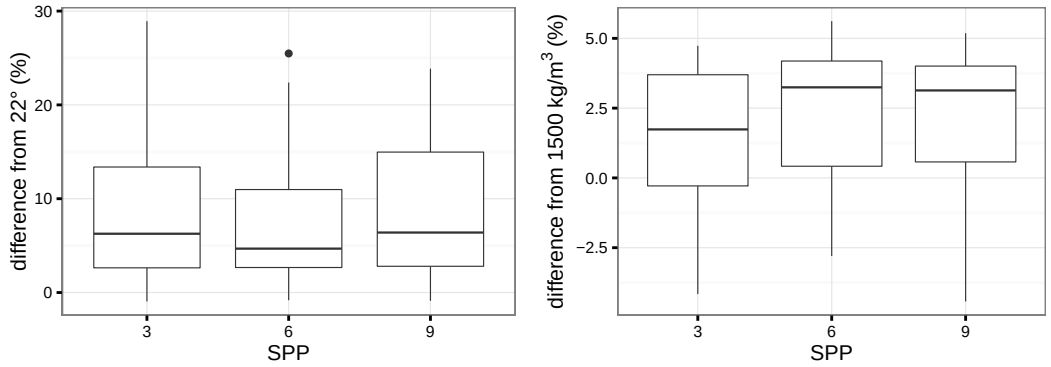

Figure 7: Boxplots of the effect of the number of samples per parameter (SPP) on the calibration outcome of the angle of repose (left) and bulk density (right).

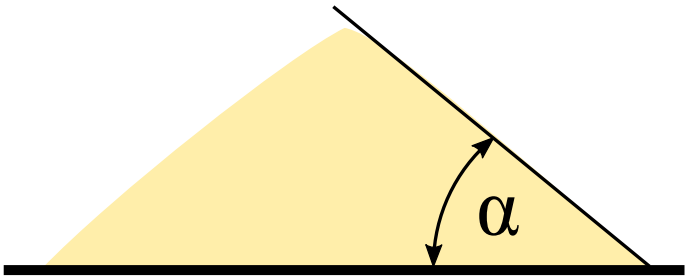

Figure 8: Side view of a bulk solid heap formed under gravity with the angle of repose α.

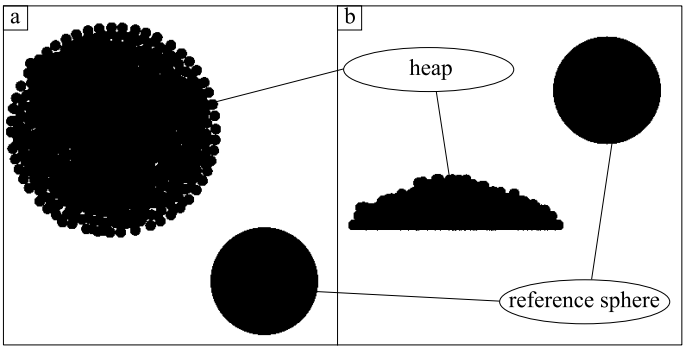

Figure 9: Top-down view (a) and side view (b) of an exemplary heap from the study.

Table 1: DEM input parameters which were fixed for all simulations where p–p is for a particle–particle contact, p–w is for a particle–wall contact and RF is the rolling friction model

Parameter	Value
Poisson's ratio	0.22
Coefficient of restitution (p–p)	0.89
Coefficient of restitution (p–w)	0.60
Viscous damping coefficient of RF (p–p)	0.25
Viscous damping coefficient of RF (p–w)	0.25

Table 2: Set parameter intervals if a parameter is included in the calibration; DENS: particle density.

Parameter	**Interval**	**Unit**	**Included?**
DENS	[2400; 2600]	$\mathrm{kg\,m^{-3}}$	always
MU_PP	[0.1; 0.3]	-	acc. to DoE
MU_PW	[0.1; 0.3]	-	acc. to DoE
RF_PP	[0.001; 0.1]	-	always
RF_PW	[0.001; 0.1]	-	acc. to DoE
YM	[4.175; 6.500]	$10^8\,\mathrm{Pa}$	acc. to DoE

Table 3: Pearson correlation coefficients between DEM optima and Kriging optima for material model and contact law parameters.

Parameter	**Correlation coefficient**
DENS	0.9465
MU_PP	0.9987
MU_PW	0.9999
RF_PP	0.9999
RF_PW	1.0000
YM	0.9969

Table 4: Pearson correlation coefficients between the response data of the DEM model and Kriging output.

Response value	**Correlation coefficient**
Angle of repose	0.7186
Bulk density	0.9413
Rayleigh time-step	0.9943

Table 5: MANOVA results; p-values and levels of significance which are indicated at the following α levels: ***/0.001, **/0.01, */0.05, ./0.1.

Factor	**Kriging**		**DEM**	
DENS	2.2e-16	***	2.2e-16	***
MU_PP	2.2e-16	***	2.2e-16	***
MU_PW	0.0219	*	0.0969	.
RF_PP	2.2e-16	***	2.2e-16	***
RF_PW	0.0001	***	8.98e-9	***
YM	2.2e-16	***	2.2e-16	***
DENS:MU_PP	0.2951		5.52e-06	***
DENS:MU_PW	0.8163		0.3043	
DENS:RF_PP	0.5870		0.0323	*
DENS:RF_PW	0.2674		0.1417	
DENS:YM	0.4780		0.0207	*
MU_PP:MU_PW	0.7802		0.0763	.
MU_PP:RF_PP	0.2428		4.99e-10	***
MU_PP:RF_PW	0.9223		0.1565	
MU_PP:YM	0.1087		0.1252	
MU_PW:RF_PP	0.9745		0.0868	.
MU_PW:RF_PW	0.7504		0.6465	
MU_PW:YM	0.4605		0.2485	
RF_PP:RF_PW	0.3476		0.5765	
RF_PP:YM	0.3305		0.5466	
RF_PW:YM	0.5656		0.5098	

Table 6: Pearson correlation coefficients between friction parameters.

Parameter combination	**Correlation coefficient**
MU_PP:MU_PW	0.239
MU_PP:RF_PP	−0.659
MU_PP:RF_PW	0.121
MU_PW:RF_PP	0.0830
MU_PW:RF_PW	0.184
RF_PP:RF_PW	0.229

Table B-1: Experimental plan of this study.

no.	WRL	SPP	MU_PP	MU_PW	YM	RF_PW
1	0	3	0	0	0	0
2	0	3	1	0	0	1
3	0	9	0	0	1	0
4	1	3	0	1	1	1
5	0	9	1	0	0	0
6	0.5	9	0	0	0	1
7	0.5	3	1	1	1	0
8	1	6	1	1	0	0
9	0.5	3	1	0	1	1
10	1	3	1	0	0	1
11	1	6	0	0	1	0
12	0	9	0	1	1	0
13	0	6	1	1	1	0
14	0	3	1	1	1	1
15	1	9	0	1	0	1
16	1	9	0	0	0	0
17	0.5	9	0	1	1	1
18	0.5	9	1	1	0	1
19	0.5	6	1	1	1	0
20	0	3	0	1	1	1
21	0	6	0	1	0	1
22	1	3	1	1	0	1
23	1	3	0	0	0	1
24	0.5	3	0	1	1	0
25	0.5	6	1	0	0	0
26	0	9	1	1	1	1
27	0	6	1	0	1	0
28	1	9	1	1	1	1
29	0.5	9	1	0	0	0
30	1	6	0	1	0	0
31	0.5	3	0	0	0	0
32	1	6	1	0	0	0
33	0.5	6	0	1	1	1
34	0.5	6	0	0	0	1
35	1	9	1	0	1	0
36	0	6	0	0	1	1
37	0	6	0	0	0	0
38	1	9	1	0	0	1
39	0.5	6	0	0	1	0
40	0.5	6	0	1	0	0
41	1	6	1	0	1	1
42	0.5	3	0	0	1	1
43	1	6	0	1	1	1
44	0.5	9	1	0	1	1
45	1	9	1	1	0	0
46	0	6	1	0	0	1
47	0	9	1	1	0	0

48	0.5	6	1	0	1	1
49	0.5	3	0	1	0	1
50	1	3	0	0	1	0
51	1	3	1	1	1	0
52	0	6	0	1	1	0
53	0	3	0	1	0	0
54	0.5	6	1	1	0	1
55	0.5	9	1	1	1	0
56	0.5	9	0	1	0	0
57	1	9	0	0	1	1
58	1	9	0	1	1	0
59	0	3	1	1	0	0
60	0	6	1	1	0	1
61	0	9	0	1	0	1
62	1	6	0	0	0	1
63	1	3	1	0	1	0
64	0.5	3	1	0	0	0
65	1	6	1	1	1	1
66	0.5	3	1	1	0	1
67	0.5	9	0	0	1	0
68	0	9	1	0	1	1
69	1	3	0	1	0	0
70	0	9	0	0	0	1
71	0	3	1	0	1	0
72	0	3	0	0	1	1